

ALMA Spectral Survey of An eruptive Young star, V883 Ori (ASSAY): I. What triggered the current episode of eruption?

JEONG-EUN LEE,^{1,2} CHUL-HWAN KIM,¹ SEOKHO LEE,³ SEONJAE LEE,¹ GISEON BAEK,¹ HYEONG-SIK YUN,³
YURI AIKAWA,⁴ DOUG JOHNSTONE,^{5,6} GREGORY J. HERCZEG,^{7,8} AND LUCAS CIEZA⁹

¹*Department of Physics and Astronomy, Seoul National University, 1 Gwanak-ro, Gwanak-gu, Seoul 08826, Korea*

²*SNU Astronomy Research Center, Seoul National University, 1 Gwanak-ro, Gwanak-gu, Seoul 08826, Republic of Korea*

³*Korea Astronomy and Space Science Institute, 776 Daedeok-daero, Yuseong, Daejeon 34055, Korea*

⁴*Department of Astronomy, University of Tokyo, 7-3-1 Hongo, Bunkyo-ku, Tokyo 113-0033, Japan*

⁵*NRC Herzberg Astronomy and Astrophysics, 5071 West Saanich Road, Victoria, BC, V9E 2E7, Canada*

⁶*Department of Physics and Astronomy, University of Victoria, 3800 Finnerty Road, Elliot Building, Victoria, BC, V8P 5C2, Canada*

⁷*Kavli Institute for Astronomy and Astrophysics, Peking University, Yiheyuan 5, Haidian Qu, 100871 Beijing, China*

⁸*Department of Astronomy, Peking University, Yiheyuan 5, Haidian Qu, 100871 Beijing, China*

⁹*Facultad de Ingeniería y Ciencias, Núcleo de Astronomía, Universidad Diego Portales, Av. Ejército 441. Santiago, Chile*

ABSTRACT

An unbiased spectral survey of V883 Ori, an eruptive young star, was carried out with the Atacama Large Millimeter/submillimeter Array (ALMA) in Band 6. The detected line emission from various molecules reveals morphological/kinematical features in both the Keplerian disk and the infalling envelope. A direct infall signature, red-shifted absorption against continuum, has been detected in CO, HCO⁺, HCN, HNC, and H₂CO. HCO⁺ and SO show large arm-like structures that probably connect from an infalling envelope to the disk. HCN and H₂CO reveal a distinct boundary between the inner and outer disk and reveal tentative spiral structures connecting the outer disk to the inner disk. HNC shows a large central emission hole ($r \sim 0.3''$) due to its chemical conversion to HCN at high temperatures. The HDO emission, a direct tracer of the water sublimation region, has been detected in the disk. Molecular emission from complex organic molecules (COMs) is confined within the HDO emission boundary, and HCO⁺ has an emission hole in its distribution due to its destruction by water. Together, these features suggest that the current episode of eruption in V883 Ori may be triggered by the infall from the envelope to the outer disk, generating a spiral wave, which propagates inward and greatly enhances the accretion onto the central star.

1. INTRODUCTION

The episodic accretion process (Hartmann & Kenyon 1996) is now accepted as the standard accretion model in low-mass star formation. Although we do not yet understand how burst accretion is driven (Fischer et al. 2022), we have reached a theoretical and observational consensus that early embedded protostars have more frequent and greater accretion burst events (Vorobyov & Basu 2015; Park et al. 2021). To explore the dynamic processes associated with episodic accretion in protostars, we have to dissect all different kinematical components, from the infalling envelope to the accreting disk, with a high spatial resolution. Decomposing individual kine-

matic components, however, is not easy during the embedded phase since multiple kinematic features are tangled together along the line of sight. Fortunately, we can utilize a variety of molecular transitions to break this degeneracy because specific molecules become abundant under particular physical conditions (e.g., Öberg & Bergin 2021; Tychoniec et al. 2021).

FU Orionis objects (FUors), which are believed to be in the burst accretion phase in the episodic accretion model, are often associated with nebulae, suggesting that they still have infalling circumstellar envelope material (Takami et al. 2018). In that condition, the infall from envelope to disk can trigger burst accretion through the disk (Vorobyov & Basu 2005, 2015). Recently, infalling streamers have been revealed by high-resolution ALMA observations of protostars (Pineda et al. 2020; Thieme et al. 2022; Mercimek et al. 2023; Lee et al.

2023), and large arm structures in FUors disks have been imaged (Takami et al. 2018). Furthermore, relatively low-velocity shocks with $\sim 3 \text{ km s}^{-1}$, which can be produced along the infalling arm structures in the dense inner envelope or at the outer disk boundary, can enhance the abundance of specific molecules, such as SO (Esplugues et al. 2014; Sakai et al. 2014; Miura et al. 2017; van Gelder et al. 2021; Lee et al. 2023). In addition, the inner disk may be heated above the water sublimation temperature of $\sim 100 \text{ K}$ by the burst accretion and can sublimate the ices of Complex Organic Molecules (COMs) together with the water ice (Bianchi et al. 2022). To resolve and analyze these physical components associated with infall and accretion, especially the water sublimation radius, FUors in the protostellar phase are likely the best targets (Lee et al. 2019).

V883 Ori is a young eruptive star, which is in transition from the Class I to Class II stage. It has a bolometric luminosity of $\sim 220 L_{\odot}$ (Furlan et al. 2016) at a distance of 388 pc (Lee et al. 2019). The water snow line was resolved in the disk indirectly with the dust continuum intensity distribution (Cieza et al. 2016, $0.1''$) and modeling of the COM emission (Lee et al. 2019, $0.1''$) and directly with water emission (Tobin et al. 2023, $0.2''$). In addition, V883 Ori is the first disk where COMs, beyond CH_3OH and CH_3CN , were detected in the midplane (van 't Hoff et al. 2018; Lee et al. 2019). In V883 Ori, the envelope still exists (White et al. 2019), and the disk is well-developed. In addition, the gaseous disk is still thick and dense enough to be mapped in molecular transitions. Previous lower-resolution ($\sim 0.5''$ to $\sim 1.5''$) ALMA observations (Ruíz-Rodríguez et al. 2017, 2022) have revealed an outflow to the NW (red-shifted, traced by ^{13}CO) and SE (blue-shifted, traced by ^{12}CO) as well as the infalling signature of red-shifted absorption against the continuum in HCN and HCO^+ . Despite careful analyses, these resolutions were unable to resolve the detailed kinematics, especially in the boundary between the envelope and the disk.

In this paper, we introduce the ALMA Spectral Survey of An eruptive Young star, V883 Ori (ASSAY). We analyze the emission distribution of various molecules and the kinematic structures traced by these molecular lines using our new high-resolution Band 6 ALMA observation of V883 Ori. Our spatial resolutions ($0.15'' \sim 0.2''$) are high enough to resolve the water sublimation radius, $r \sim 0.3''$, in the disk surface, and the maximum recoverable sizes ($1.6''$ to $3.7''$ equivalent with 600 au to 1500 au) are large enough to cover the infalling inner envelope. Above all, the complete frequency coverage

from ~ 221 to $\sim 275 \text{ GHz}$, with a decent velocity resolution ($\sim 0.6 \text{ km s}^{-1}$), allows us to utilize various molecules to explore the different physical/kinematical structures. As a result, our work will complement the investigation by Ruíz-Rodríguez et al. (2022).

We describe our observations and data reduction in Section 2, and we analyze the spatial distributions of detected molecules in Section 3. The different kinematics traced by specific molecules are explored in Section 4. In Section 5, we stitch the phenomena found in Sections 3 and 4 together to understand how the different physical components are associated with the most recent outbursting episode. Finally, the summary is provided in Section 6.

2. OBSERVATION

The ASSAY (ALMA Spectral Survey of An eruptive Young star, V883 Ori) observations were carried out in band 6 during Cycle 7 (2019.1.00377.S, PI: Jeong-Eun Lee). The spectral survey covers from ~ 221 to $\sim 275 \text{ GHz}$ with three Science Goals (SGs), which have five tunings each and four spectral windows (SPWs) per tuning, resulting in 60 SPWs in total. Each SPW covers a bandwidth of 933.5 MHz and a spectral resolution of 488.281 kHz ($0.66 \sim 0.53 \text{ km s}^{-1}$). The observation logs are listed in Table 1.

The calibration was performed using the CASA pipeline (6.2.1.7) with a quasar, J0423-0120, as the bandpass and flux calibrators and a quasar, J0529-0159, as the phase calibrator. Three phases and one amplitude self-calibrations were carried out for each SG. V883 Ori has emission from many molecular lines, and thus, it is not easy to find line-free channels in the UV plane. Therefore, the spectral line images were cleaned with the continuum, and the line channels were found by requiring either strong extended emission (CO, HCN, HCO^+ , etc) or, for the COMs emission, a signal higher than the 3σ RMS level in the averaged spectra within an aperture of $0.3''$. Next, the continuum images, cleaned using the line-free channels, were adopted for the self-calibration. The self-calibration increases the S/N of the continuum images by a factor of 6. The S/N of line data was only slightly improved, however, as the original calibration provided RMS levels close to the theoretical values.

The spectral images were cleaned using the Briggs weighting (robust = 0.5) for SGs 1 and 2 and the Natural weighting for SG 3, to achieve a better resolution. The beam sizes and RMS noise levels for all SPWs are provided in Table A1 in the Appendix. The continuum was subtracted in the image space, and the continuum level is automatically measured using STATCONT (Sánchez-

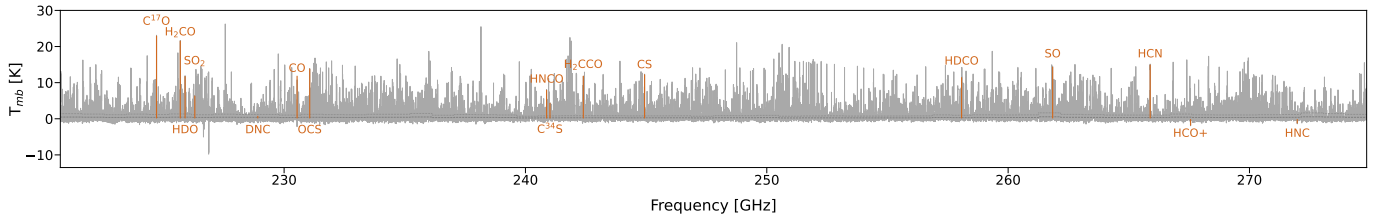


Figure 1. The entire ALMA Band 6 spectra obtained by the spectral scan mode. More than 4500 lines are detected above the three-sigma level. The absorption lines around 226 GHz are due to CN. The orange-colored spectra indicate the molecular lines to be studied in this work, and they are listed in Table 2. The spectra were extracted over the COMs emission region ($\sim 0.3''$ in radius), and thus, some molecular lines, such as the HCO^+ and HNC lines, which have emission holes inside the water sublimation radius, do not show lines in this plot.

Table 1. Observation logs

SGs	Frequency ranges (GHz)	Obs. Date	Baselines	Num. of Antenna	Int. Time (on-source, min)
SG1	220.70– 238.86	2021/05/10	15.1 m – 2.5 km	44	37.9
		2021/11/09	41.4 m – 3.4 km	47	37.9
SG2	238.70– 256.86	2021/06/28	15.1 m – 2.0 km	40	22.7
		2021/11/11	41.4 m – 3.6 km	47	22.7
SG3	256.70 – 274.86	2021/11/15	41.4 m – 3.6 km	52	50.6

Monge et al. 2018). To check the consistency across the 60 SPWs, all SPWs were convolved into a beam of $0.25'' \times 0.15''$ (-77°), similar to the poorest resolution of the second SG. The averaged continuum intensity within an aperture of $0.3''$ (red crosses) is plotted in Figure A1 in the Appendix. The continuum images using the STATCONT show consistent values within individual SPWs, confirming that the calibrations and the continuum subtraction were well carried out. The second SG shows lower fluxes than the other two SGs but remains within the calibration uncertainty of 5% (Francis et al. 2020).

3. SPATIAL DISTRIBUTION OF MOLECULAR EMISSION

Our ALMA observations detect about 4600 lines (Figure 1), mostly from COMs. The spectra presented in Figure 1 have been extracted by the PC1-filtering method developed using the Principle Component Analysis (PCA) applied to the cube data of isolated strong COMs lines (Yun & Lee 2023). PCA is one of the multivariate statistics that access the common features veiled in the variation of data (Jolliffe 1986), and recently, PCA has been applied to ALMA observations to assess the distribution of molecular lines in position-velocity spaces (PCA-3D, Okoda et al. 2021). Here, PC1 is the first principle component derived from the PCA and represents the most common kinematic

and spatial emission structures of COMs. In V883 Ori, COMs emit mainly in the disk with the Keplerian rotation (Lee et al. 2019; Yun & Lee 2023). Therefore, PC1 contains the kinematic information (i.e., Keplerian rotation) that can be used to correct the velocity shifts of spectra. We apply the PC1-filtering method to the entire frequency range covered by our spectral survey to extract the spectra presented in Figure 1. Detailed analyses of the extracted COMs spectra will appear in a separate paper (Jeong et al. submitted).

In this paper, we focus on simple molecules, which are composed of less than 6 atoms, while selected images of several COMs are also presented. The simple molecules used for this work are marked in Figure 1 in the orange color and listed in Table 2. There are many more lines of simple molecules, detected by our spectral survey but not covered by this work. We use the self-calibrated original cube data, without the beam convolution used in Section 2 to check for the consistency of all SPWs. We analyze both the 2-D emission distribution at high angular resolution and the kinematics traced by different molecules after identifying detected simple molecules and checking their contamination by other lines based on the spectra presented in Figure 1.

The physical parameters of V883 Ori are adopted from the literature as follows. The distance of V883 Ori has been updated recently to 388 ± 16 pc (Lee et al. 2019).

The systematic velocity of V883 Ori is 4.3 km s^{-1} (Cieza et al. 2016). The inclination inferred from the ratio between the disk semi-major and semi-minor axes is $38.3 \pm 1^\circ$ (Cieza et al. 2016), and the position angle of the rotation axis, which is the same as the outflow axis, is $\sim 120^\circ$ (Cieza et al. 2016; Ruíz-Rodríguez et al. 2017). The blue-shifted outflow is located in the southeast direction from V883 Ori. Thus, the southeast part of the disk is facing toward us. Cieza et al. (2016) obtained that the disk radius, traced by the $\text{C}^{18}\text{O } J=2-1$, is $338 \pm 25 \text{ au}$, while the dust disk is limited within a radius of 116 au . Note that the continuum emission extends up to $0.''8$ in our observations as shown in the contours in Figure 2 because of the larger maximum recoverable scale compared to that in Cieza et al. (2016). Based on the new distance measurement, the central mass is $1.2 M_\odot$, estimated using the Keplerian rotation traced by the C^{18}O and C^{17}O lines (Cieza et al. 2016; Lee et al. 2019).

To investigate the emission distribution and associated kinematics of simple molecules, we utilized various moment maps. *Moment 0* corresponds to integrated intensity, *Moment 1* shows the intensity-weighted velocity, *Moment 8* reveals the peak intensity (the maximum value across the channels), and *Moment 9* represents the peak velocity (the velocity of the peak intensity). Note, therefore, that in this paper, the moment 0 and 1 maps follow the standard mathematical definition, however, the moment 8 and 9 have been redefined. Here the moment 8 and 9 maps are defined such that they report similar information as in the moment 0 and 1 maps, respectively.

We create the moment maps of each molecule by clipping out values below 4σ . The value of the RMS of each SPW is listed in Table A1. Moment 0 and 1 maps are created by integrating the emission over a range of velocity so that there are chances of contamination by other unidentified lines, hyperfine structure lines, or multiple kinematic components. However, moment 8 and 9 maps better present the distribution of the dominating line emission. In this work, we use conventional moment 0 and 1 maps for most lines, but moment 8 and 9 maps are adopted if necessary.

The most prominent common feature from the moment 0 maps is the emission hole inside $r \sim 0.1''$. This feature has already been well recognized in the previous ALMA Band 7 observations (Lee et al. 2019), and it is caused by the optically thick dust continuum emission, which blocks all the molecular emission (Lee et al. 2019; Ruíz-Rodríguez et al. 2022). The emission size varies

significantly between molecules; CO ($> 4''$) and HCO^+ ($\sim 3''$) have the largest and second largest emission regions, respectively, while SO_2 ($\sim 0.5''$) has the smallest emission size. Details of the morphological distribution of each molecular emission are presented in the following subsections.

3.1. Water sublimation region

HDO (Figure 2): V883 Ori is the only disk source where the water snowline is resolved via water emission itself (Tobin et al. 2023). The moment maps of HDO are presented in Figure 2; the HDO line adopted in this figure is the same as Tobin et al. (2023) used. A stronger emission is seen in the southeast half because the southeast part faces us due to the disk inclination. The line profile in the right panel was extracted over all pixels with intensity above 4σ after correcting the velocity shift caused by the Keplerian rotation at individual pixels. The strong line next to the HDO line is a $\text{CH}_3^{13}\text{CHO}$ line.

The boundary of the HDO emission ($r \sim 0.3''$) defines the water sublimation radius *in the disk surface*. Within the disk, the water sublimation radius varies with disk height to form an axis-symmetric water sublimation surface. In particular, the water sublimation radius in the disk midplane is referred to as the *water snow line*. The largest water sublimation radius, as traced by HDO, is about 120 au ($\sim 0.3''$). On the other hand, the water snow line is smaller than 120 au ; Cieza et al. (2016) and Lee et al. (2019) suggested a radial size $\sim 40 \text{ au}$ for the water snow line in V883 Ori based on the dust continuum intensity profiles and modeling of the $^{13}\text{CH}_3\text{OH}$ line emission distribution, respectively. However, Tobin et al. (2023) argued that the snowline of V883 Ori is $\sim 80 \text{ au}$. A better model is required to constrain the water snow line more accurately. In this paper, therefore, we refer to the water sublimation radius of 120 au as the boundary of the HDO emission, which must be located on the disk surface.

3.2. Molecular emission confined within the water sublimation region

HDCO, HNC, OCS, C^{34}S , SO_2 , and COMs (Figures 3, 4, and 5): The five simple molecules in Figure 3 and COMs in Figure 4 trace mainly the water sublimation front and the Keplerian rotation of the inner disk distinctively, as seen in their moment maps.

Figure 4 shows only the integrated intensity (moment 0) maps of 11 selected COM lines, including H_2CCO , since moment 1 maps of these lines have similar trends to those of HDO. More COMs have been detected in our spectra extracted over the disk (Figure 1), but the

Table 2. List of simple molecules

No.	molecular transition	Frequency [GHz] (SPWs)	E_u [K]
1	HDO 3(1,2)-2(2,1)	225.89672 (SG1 SPW6)	167.6
2	HDCO 4(3,2)-3(3,1)	258.07094 (SG3 SPW2)	102.6
3	HNCO 11(1,11)-10(1,10)	240.87573 (SG2 SPW3)	112.6
4	OCS 19-18	231.06099 (SG1 SPW12)	110.9
5	C ³⁴ S 5-4	241.01609 (SG2 SPW3)	27.8
6	SO ₂ 14(3,11)-14(2,12)	226.30003 (SG1 SPW7)	119.0
7	H ₂ CO 3(1,2)-2(1,1)	225.69775 (SG1 SPW6)	33.4
8	HCN 3-2 ^a	265.88643 (SG3 SPW11)	25.5
9	HNC 3-2	271.98114 (SG3 SPW17)	26.1
10	DNC 3-2	228.91049 (SG1 SPW10)	22.0
11	C ¹⁷ O 2-1 ^b	224.71419 (SG1 SPW5)	16.2
12	CO 2-1	230.53800 (SG1 SPW11)	16.6
13	HCO ⁺ 3-2	267.55763 (SG3 SPW12)	25.7
14	CS 5-4	244.93556 (SG2 SPW7)	35.3
15	SO 7(6)-6(5)	261.84372 (SG3 SPW6)	47.6
16	H ₂ CCO 12(3,10)-11(3,9)	242.39845 (SG2 SPW5)	193.0

^aHCN 3-2 has 5 hyperfine components. We refer to [Ahrens et al. \(2002\)](#) for their rest frequencies.

^bC¹⁷O 2-1 has 9 hyperfine components. We refer to [Tin e et al. \(2000\)](#) for their rest frequencies.

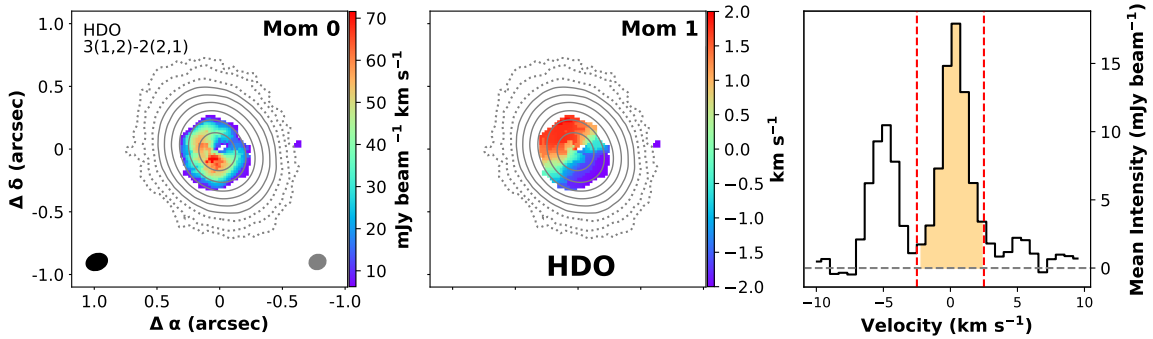


Figure 2. Moment maps and line profile of HDO 3(1,2)-2(2,1), which is the strongest line among 4 HDO lines covered by this spectral survey. Contours in the left (moment 0) and middle (moment 1) present the continuum emission distribution extracted from the SG3 data set, which has the best resolution. The contour levels are 5, 10, 25, 50, 100, 200, 400, 800, and 1600 σ ($\sigma = 0.023$ mJy beam⁻¹). The first three contours for low intensities are plotted with dotted lines. The boundary of the HDO emission shown in the integrated intensity map (moment 0) is the water sublimation radius *in the disk surface*. The disk rotation is clearly seen at the moment 1 map. The ellipses in the lower left and right corners at the moment 0 map represent the beam sizes of the HDO line and continuum, respectively. The contour levels and the beam size of the continuum image are the same in all other figures. The unit of moment 0 and 1 maps are mJy beam⁻¹ km s⁻¹ and km s⁻¹, respectively. The line profile in the right panel is averaged over all pixels with an intensity greater than 4 σ after correcting the velocity shift caused by the Keplerian rotation at individual pixels. The velocity range used for the moment maps is marked with the dashed red vertical lines.

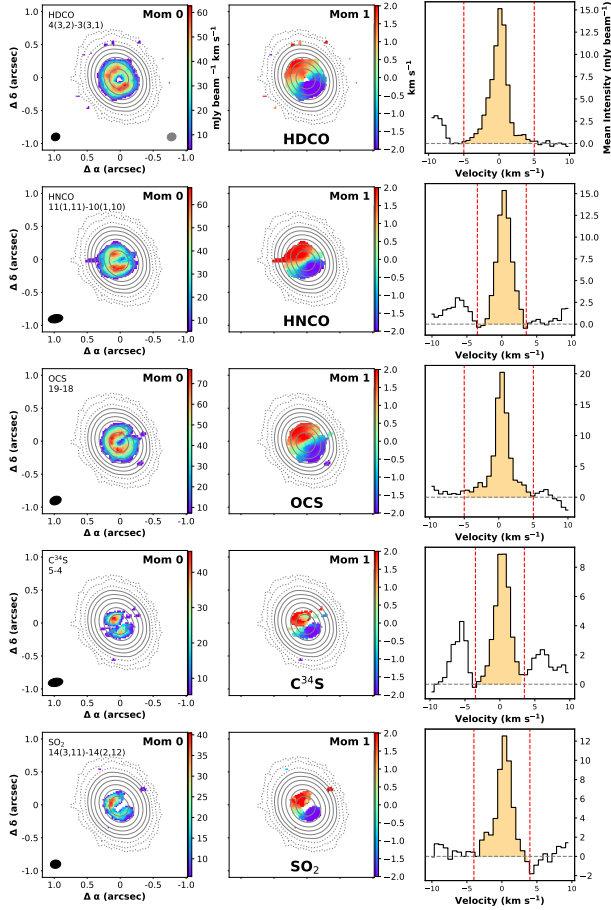


Figure 3. Moment maps and line profiles of the spectral line showing compact distribution (HDCO, HNCO, OCS, $C^{34}S$, and SO_2 lines), whose size is similar to the water sublimation radius. Contour levels for the continuum are the same as in Figure 2, and the spectra in the third column are extracted as explained in Figure 2.

weak lines of some low-abundance COMs are not strong enough to produce nice 2-D images. Over our frequency coverage, COMs have multiple transitions, among which the strongest line in SG3 was selected for their moment maps in each species for the best resolution. If the lines in SG3 are too weak, we used the strongest lines either in SG1 or SG2. Table 3 lists the COMs lines used for the moment 0 maps in Figure 4.

All emissions from COMs, as well as HDCO, HNCO, and OCS, arise exclusively from the central region within the water sublimation radius. Therefore, these molecules could be used as alternative tracers of the water sublimation region in the disk.

$C^{34}S$ shows somewhat different emission distributions from the other molecules. $C^{34}S$ (also HNCO in Figure 3) has two elongated emission blobs. However, this is not a real emission feature of this molecule, rather the

very elongated beam shape obtained by SG2 distorts the emission feature.

Figure 5 shows the comparison between the original CH_3OH image and the image convolved with the elongated beam obtained by SG2 to demonstrate the $C^{34}S$ image does not show a real emission distribution. The two disconnected emission blobs seen in HNCO, $C^{34}S$, H_2CCO , $CH_3^{18}OH$, $CH_3O^{13}CHO$ are due to the beam shape.

SO_2 , known as a shock tracer, seems to have stronger emission toward the north than in the south. Similar characteristics are exhibited by some of the COMs lines, such as $^{13}CH_3OH$ (see Figure 4). This may imply that a shock event existed within the inflow motion to the northern part of the disk, as hinted by the HCO^+ channel map (see Section 4.1).

3.3. Inner and outer disks

H_2CO and HCN (Figure 6): These molecules trace the largest gas disk at the size of $r \sim 0.8''$. Disk emission traced by these molecules appears to be divided into two regions: one confined at the center within the water sublimation radius of $0.3''$ and the other confined within a ring structure between $\sim 0.5''$ and $0.8''$, where the dust continuum intensity still exists. Although the emission seems confined within the disk, these two molecular lines also trace the infalling envelope, as seen in the redshifted absorption against the continuum (see Section 4.3).

The HCN line has hyperfine structures as marked in its line profile (the third column of the second row in Figure 6). These hyperfine components contaminate the moment 1 map of HCN 3-2. Therefore, the moment 9 map better presents the velocity distribution of the peak intensity for the main component. The HCN map also shows arm-like structures connecting the outer disk and the inner disk (See section 4.1 for the detailed discussion).

3.4. A ring structure in the outer disk

HNC and DNC (Figure 6): HNC and DNC trace only the ring structure at the outer disk. The ring is the most prominent in HNC. The size of the emission hole of HNC is found to be similar to the water sublimation radius. Fraser et al. (2001) reported that water would sublimate at temperatures greater than ~ 100 K for interstellar conditions. At the emission hole, HNC could therefore be converted to HCN via the reaction $HNC + H \rightarrow HCN + H$ (with an energy barrier lower than 200 K, Hirota et al. 1998; Graninger et al. 2014; Jin et al. 2015; Hacar et al. 2020) because this reaction is efficient above 40 K. A chemical time scale also depends on the hydrogen number density and, thus, could be much

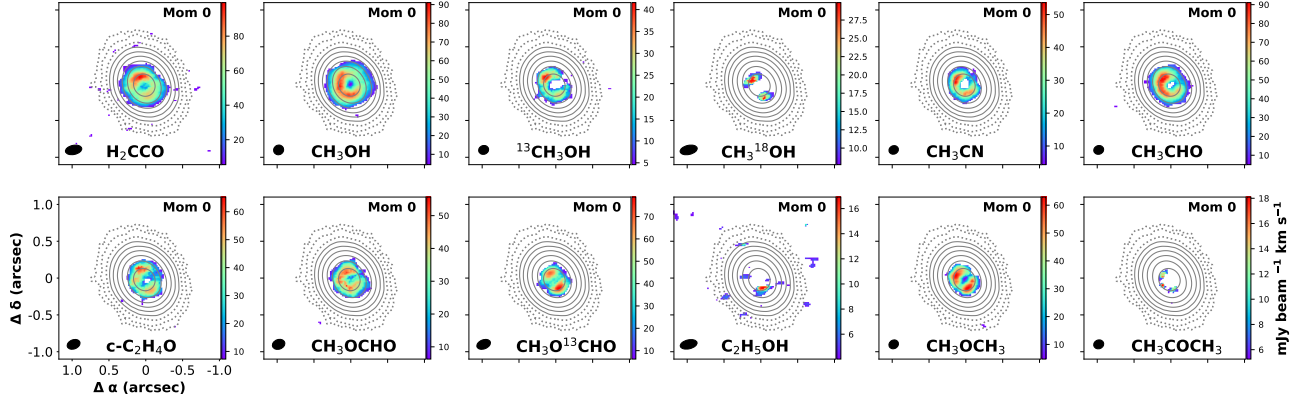


Figure 4. Integrated intensity (moment 0) maps of selected COMs. The adopted line transition of each COM is listed in Table 3

Table 3. List of selected COMs

No.	molecular transition	Frequency [GHz] (SPWs)	E_u [K]
1	CH ₃ OH 2(1,1)-1(0,1)	261.80574 (SG3 SPW06)	28.0
2	¹³ CH ₃ OH 9(-1,9)-8(0,8)	268.63544 (SG3 SPW14)	107.5
3	CH ₃ ¹⁸ OH 9(-0,9)-8(1,7)E, vt=0	250.14877 (SG2 SPW13)	112.9
4	CH ₃ CN 14(4)-13(4)	257.44813 (SG3 SPW1)	207.0
5	CH ₃ CHO 14(7,8)-13(7,7)E, vt=0	269.83409 (SG3 SPW15)	207.5
6	c-C ₂ H ₄ O 8(1,8)-7(0,7)	235.10502 (SG1 SPW16)	52.4
7	CH ₃ OCHO 19(3,17)-18(3,16)E	225.60882 (SG1 SPW06)	116.7
8	CH ₃ O ¹³ CHO 22(1,22)-21(0,21), v=1-1	236.27864 (SG1 SPW18)	132.8
9	C ₂ H ₅ OH 15(1,15)-14(0,14), anti	251.56647 (SG2 SPW15)	97.6
10	CH ₃ OCH ₃ 24(5,20)-24(4,21)EE	260.00439 (SG3 SPW04)	308.9
11	CH ₃ COCH ₃ 26(1,25)-25(2,24)EA	268.28371 (SG3 SPW13)	181.7

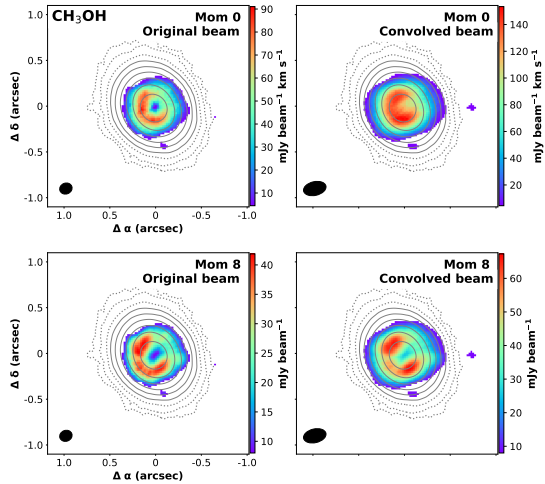


Figure 5. Comparison between the original high-resolution images (left) and the images convolved with the elongated beam of the SG2 observations (right). The beam is located in the lower left corner of each image.

shorter in the inner disk than in the outer disk, resulting in a clear HNC ring structure. More detailed chemical models are needed to investigate this conversion (Long et al. 2021).

Figure 7 shows the intensity distribution comparison between the HCN and HNC lines; the HNC emission is missing within the hot inner disk, while the HCN emission shows two peaks, at 0.2'' and 0.7''. The velocity distribution of the ring mainly follows the disk rotation well (see Section 4).

3.5. A tracer of the dust disk

C¹⁷O (bottom panels of Figure 6): In contrast to the other presented lines, except for the emission hole inside 0.1'', the C¹⁷O J=2-1 emission distribution (moment 0) is most consistent with the dust emission without any substructure. Its outer boundary is close to the peak of the HNC emission (see the blue dashed line in Figure 7). The high dust opacity causes the missing emission at the

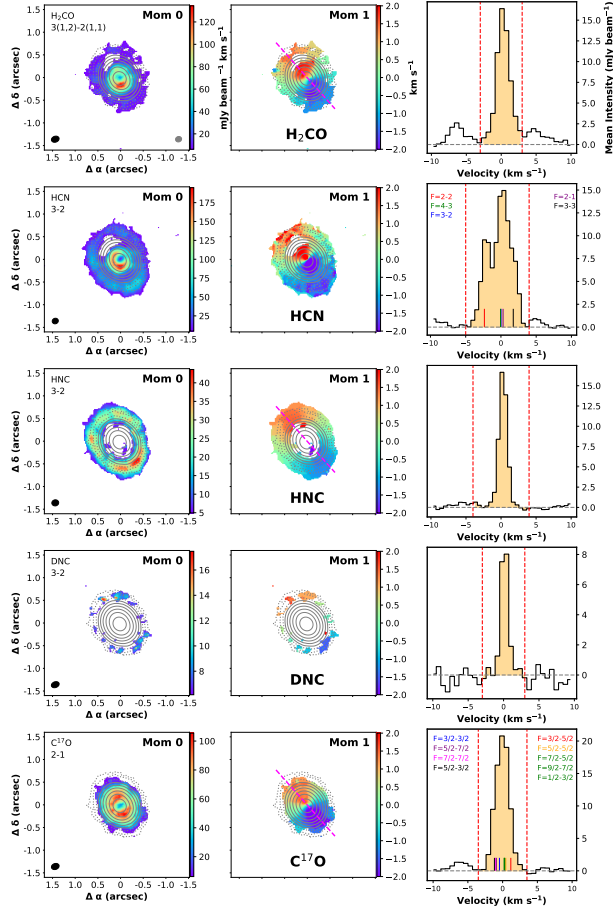


Figure 6. Moment maps and line profiles of molecules (H_2CO , HCN , HNC , DNC , and C^{17}O) showing emission in the outer disk. Contour levels for the continuum are the same as in Figure 2. Moment 1 map of HCN is affected by its hyperfine structure, whose components are marked in the HCN averaged line profile with vertical solid lines. C^{17}O $J=2-1$ also has a hyperfine structure, as marked in its averaged line profile, but they are not resolved with our velocity resolution. The magenta dashed lines at the moment 1 maps of H_2CO , HNC and C^{17}O indicate the cut used for the PV diagram in Figure 15. The spectra in the third column are extracted as explained in Figure 2.

center. In addition, the Keplerian rotation is well recognized (see its moment 1 map in Figure 6), as seen in the C^{17}O $J=3-2$ emission presented by Lee et al. (2019) (see Section 4.2). C^{17}O is known to be a good tracer of disk (van’t Hoff et al. 2020) since its lines are optically thin. In addition, the temperature of the V883 Ori disk must be greater than the CO sublimation temperature (~ 20 K) in most regions of the disk because of its high central luminosity and viscosity heating in the disk midplane.

3.6. Large-scale structures in the envelope

CO , HCO^+ , CS , and SO (Figure 8): The emission of these molecules appear at scales larger than $1''$, and thus,

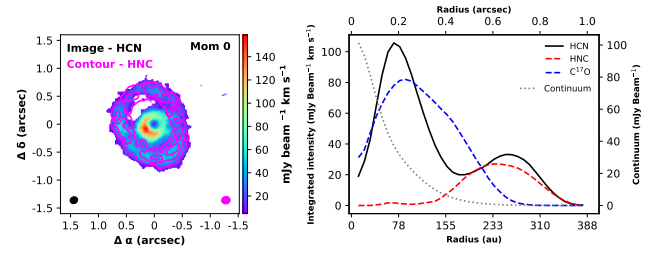


Figure 7. Integrated intensity distribution comparison between the HCN and HNC lines. In the left panels, the magenta contours show the moment 0 map of the HNC line on top of the moment 0 image of HCN . Contour levels for the molecule are 15, 25, and 35 $\text{mJy beam}^{-1} \text{ km s}^{-1}$. The ellipse in the lower left corner represents the beam size of images, while the ellipse in the lower right corner shows the beam size of contours. The right panels present the azimuthally averaged intensity profiles of HCN (black solid line) and HNC (red dashed line) as well as the continuum (dotted grey line). The blue dashed line shows the C^{17}O line intensity profile for comparison.

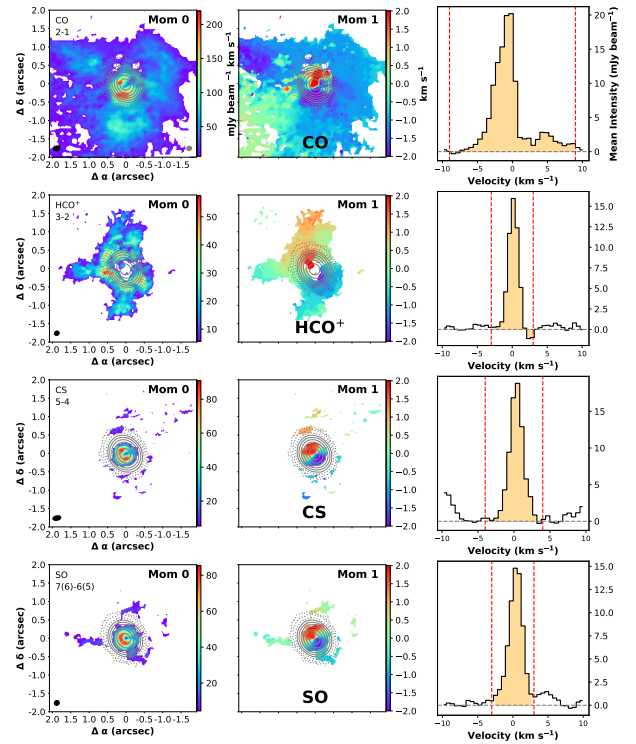


Figure 8. Moment maps and line profiles of molecules (CO , HCO^+ , CS , and SO) having extended-envelope components in the maps. Contour levels for the continuum are the same as in Figure 2, and the spectra in the third column are extracted as explained in Figure 2.

likely trace the envelope material of V883 Ori, whose morphology is far from spherically symmetric. First, the CO J=2–1 map shows a clumpy and complex emission distribution. The moment 1 map shows a similar velocity feature to the map of the same CO line reported by Ruíz-Rodríguez et al. (2017); the CO emission traces the blue-shifted outflow cavity walls with a wide opening angle. The HCO⁺ emission is strongest along a ring-like structure, which is consistent with the HNC emission distribution (left panel of Figure 9).

Within the central region of $\sim 0.3''$, the HCO⁺ emission is missing, probably a combination of its destruction by H₂O (Leemker et al. 2021) and the dust optical depths effects (Ruíz-Rodríguez et al. 2022). Strong CS and SO emission is also confined within the water sublimation radius, although extended and faint large emission structures are seen beyond the water sublimation radius. These molecular lines show the disk rotation within the water sublimation radius.

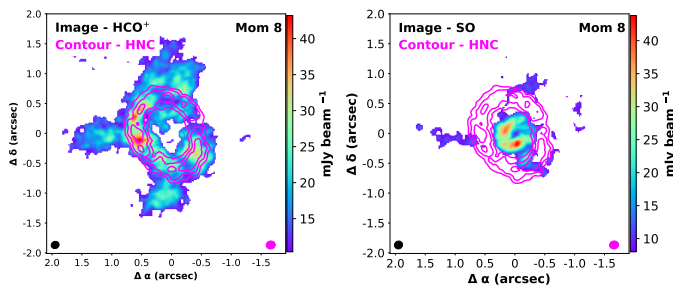


Figure 9. Comparisons between HNC and HCO⁺ (left) or HNC and SO (right). The ellipse in the lower left corner represents the beam size of images, while the ellipse in the lower right corner shows the beam size of contours. The contour levels are 14.2, 21.2, and 29.2 mJy beam⁻¹.

Figure 10 compares the integrated intensity distributions of the HCO⁺ and HDO lines; the HDO emission lies well inside the HCO⁺ emission hole, indicative of a chemical anti-correlation. The small peak of the HCO⁺ intensity profile around $0.1''$ in the right panel (solid black line) may be caused by the contamination of a CH₃OCHO line in the vicinity of the HCO⁺ line although the averaged HCO⁺ line profile over the whole cube image does not show a blended feature in Figure 8. This contamination can happen only inside the water sublimation radius since all COMs are frozen on grain surfaces beyond the water sublimation radius.

HCO⁺ emission shows several large arm-like structures extending from the outer disk. SO also shows faint arms (right panel of Figure 9) with a length of $\sim 1''$, but the strong emission is confined only within the emission hole of the HCO⁺. Therefore, the strong SO emis-

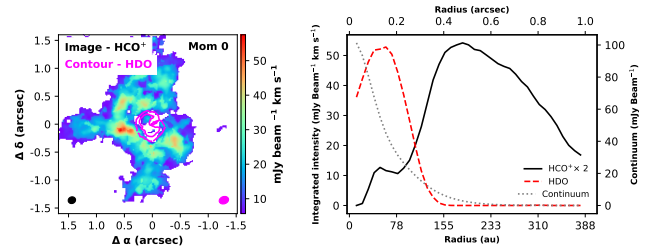


Figure 10. Integrated intensity distribution comparison between the the HCO⁺ and HDO lines. In the left panels, the magenta contours show the moment 0 maps of the HDO line on top of the HCO⁺ moment 0 image. Contour levels are 15 and 45 mJy beam⁻¹ km s⁻¹. The ellipse in the lower left corner represents the beam size of images, while the ellipse in the lower right corner shows the beam size of contours. The right panels present the azimuthally averaged intensity profiles of HCO⁺ (black dotted line) and HDO (red dashed line) as well as the continuum (dotted grey line). Intensity profiles are scaled up and down to match the peak values for better comparisons.

sion distribution coincides with the HDO emission. The overlaid HNC emission distribution on the SO image clearly demonstrates the SO emission is confined within the water sublimation radius with three faint large arm structures. The SO arms stretch to the east and the northwest along corresponding HCO⁺ structures. The southern SO arm does not show a clear counterpart in HCO⁺. CS shows the same compact emission in the disk as SO, while the faint extended structures traced by CS do not coincide with those in SO.

These arm-like structures are in Figure 9, possibly streamers infalling from the envelope to the disk. Recently, narrow structures that asymmetrically feed gas from the envelope to the scale of the circumstellar disks (Pineda et al. 2020; Bianchi et al. 2022; Thieme et al. 2022; Lee et al. 2023) have been detected in various molecular tracers and called infalling streamers. According to other observations (Valdivia-Mena et al. 2022; Lee et al. 2023), SO is likely a good tracer of infalling streamers from the inner envelope to the disk. However, the velocity resolution of our data is not high enough to study the kinematics of the arm-like structures in detail. To confirm whether the SO weak emission structures are tracing the true infalling streamers, we need a better spectral resolution as well as a better sensitivity.

4. KINEMATICS AND DYNAMICS

4.1. Large arm-like and small spiral-like structures

As indicated above, HCO⁺ and SO show $\sim 1''$ scale of arm-like structures connected to the disk (see Figure 9). The velocity distributions (see moment 1 maps in Figure 8) along the three arms of HCO⁺ and SO show

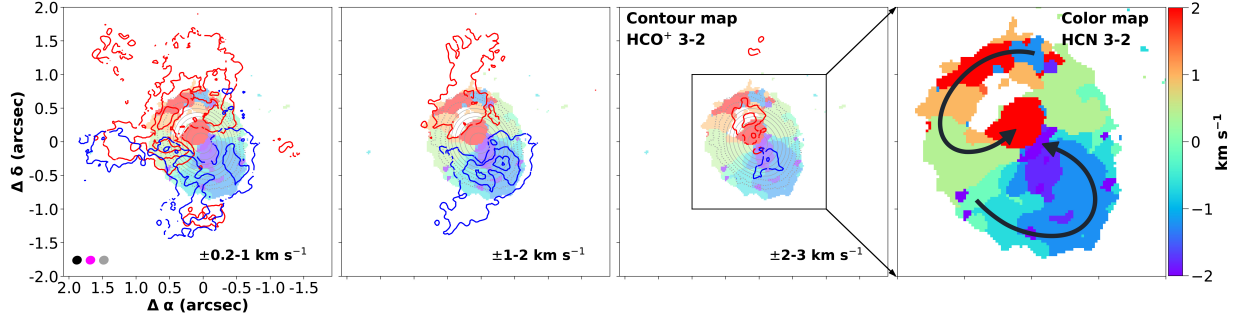


Figure 11. The channel maps of HCO^+ (contours) on top of the moment 9 map of HCN (colors). Red and blue contours in each panel are the HCO^+ intensity integrated over the velocity ranges denoted in the lower right. Contour levels are from 5.7 to 57.5 $\text{mJy beam}^{-1} \text{ km s}^{-1}$ in step of 13.0 $\text{mJy beam}^{-1} \text{ km s}^{-1}$. The ellipses in the lower left represent the beam size of the HCN (black), HCO^+ (magenta), and continuum (gray), respectively. The rightmost panel presents the zoom-in moment 9 map of HCN with bolder colors.)

velocity gradients toward the disk. The HCO^+ channel maps are presented as contours in Figure 11; the outside-in flows are detected at both red- and blue-shifted velocities. Several high-resolution images by ALMA show relatively large-scale arm structures resembling those detected here (e.g., Pineda et al. 2020; Lee et al. 2023, for IRAS 03292+3039, IRAS 04239+2436, respectively).

There are also hints of spiral-like structures connecting the outer and inner disks in H_2CO and HCN. The peak velocity map of HCN 3-2 (see the rightmost panel in Figure 11 for a zoom-in image) shows outside-in flow-like structures both in the blue- and red-shifted velocities, as guided by the arrows. Like HCN, the peak intensities of H_2CO also distribute along the outer ring-like region, and spiral-like structures seem to exist in the south and north of the outer disk along the black dots in Figure 12. These types of spiral arms have been resolved within dust disks (Lee et al. 2020). Such spiral structure within the disk can be mainly induced by the gravitational instability of the disk or interaction with a companion (Lee et al. 2020).

The comparison between the observed and modeled moment 9 maps of C^{17}O , HCN, H_2CO , and HCO^+ show some difference (Figure 12). The model velocity map was first generated using the disk parameters (i.e., inclination and position angle) and the central mass (see Section 3). Then, it was convolved with the observational spatial and spectral resolutions and masked by the emission region of each molecule for comparison. The C^{17}O moment 9 map, which is the best tracer of the Keplerian disk, is consistent with the model. In the moment 9 maps of other molecular lines, some differences are notable. It is seen especially in the outer disk in HCN, in the inner disk in H_2CO , and along the arm-like structure in HCO^+ .

For a simple examination of the spiral structures, we follow the analysis presented by Lee et al. (2020) to fit

the peak intensity positions of HCN along the spiral arms in the polar coordinates with two spiral shapes: the logarithmic spiral with $R = R_0 e^{a\theta}$, developed by the gravitational instability and the Archimedean spiral with $R = R_0 + b\theta$, induced by the interactions with a companion. Figure 13 shows fits for these spiral profiles to the two arms of HCN. The northern arm does not reveal a spiral profile, while the southern arm is well-fit. It is unclear, however, which spiral shape fits better the spiral arm.

The gravitational instability in the disk can be quantified by the Q parameter (e.g., Toomre 1964; Kratter & Lodato 2016):

$$Q = \frac{c_s \Omega}{\pi G \Sigma}, \quad (1)$$

where c_s is the sound speed, Ω is the Keplerian angular velocity, G is the gravitational constant, and the Σ is the disk surface density. The disk should be gravitationally unstable when $Q < 1$. If we calculate the Q parameter with the surface density profile of Cieza et al. (2018) and the *current* temperature profile (i.e., 100 K at 39 au Lee et al. 2019), it is greater than 2 at all radii and ~ 7 at 200 au (see the red line in Figure 14). Therefore, currently, the disk appears gravitationally stable.

The spiral structure, however, may have developed prior to the burst accretion. The disk must have a lower temperature profile before burst accretion. If the snow-line was located at 4 au, then $Q < 2$ at $r < 100$ au and $Q \sim 3.5$ at 200 au (see the blue line in Figure 14). In addition, recent works (Alves et al. 2019; Díaz Rodríguez 2021) show that Class I disks with $Q > 4$ can have prominent spiral structures. Therefore, the spiral arms in the disk of V883 Ori could have been developed before the current outburst event. However, the spiral-like structures do not appear in the dust continuum and C^{17}O emission. Therefore, the spiral arms detected in the

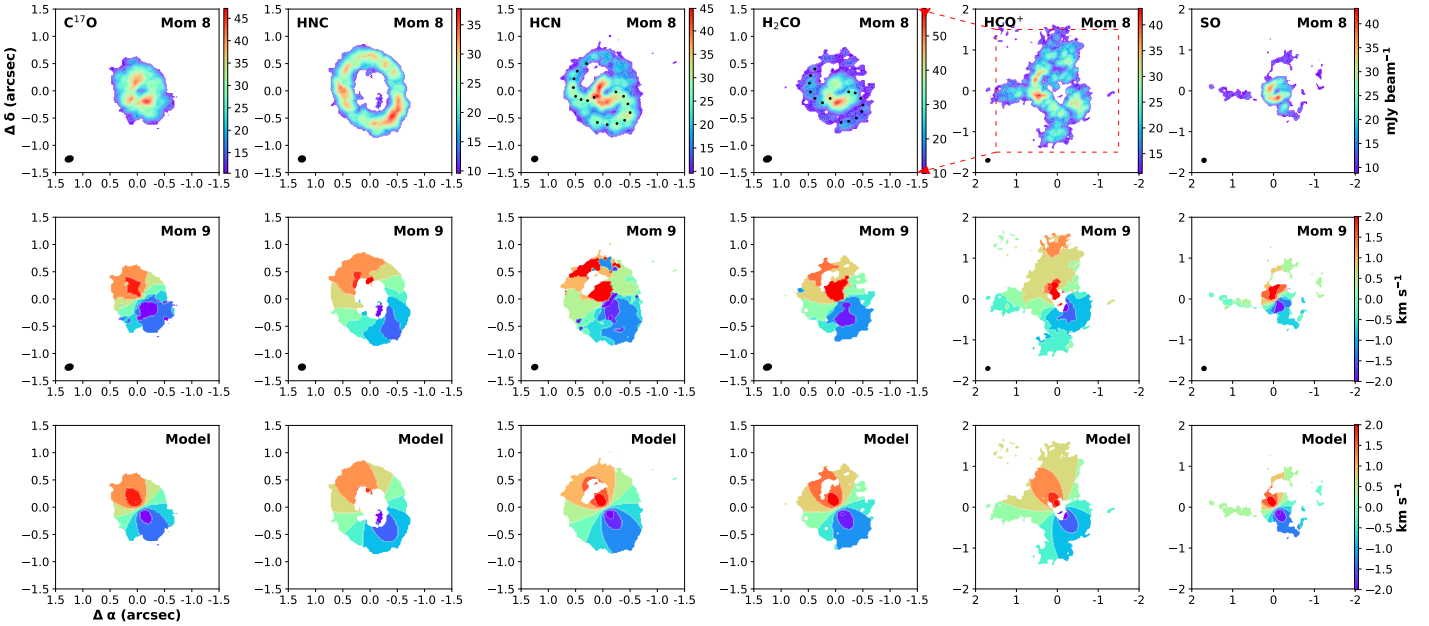


Figure 12. The observed moment 8 and 9 maps and the modeled moment 9 maps. The model is based on Keplerian rotation around a $1.2 M_{\odot}$ source with an inclination of 38° and a PA of 120° . The black dots are plotted at the moment 8 maps of HCN and H_2CO to guide along the spiral-like structures.

shock tracers, HCN and H_2CO are probably the chemical footprint that remains after the disk was stabilized.

Despite these morphological features, the velocity resolution of our data is not high enough to robustly examine the kinematics of the large arm-like structures beyond the disk. The S/N ratio of the images is not high enough to confirm the spiral structure within the disk either. Therefore, we need images with a high spatial and spectral resolution and a higher S/N ratio to inspect these features in more detail.

4.2. Disk Rotation

The $C^{17}O$ line emission appears consistent with the smooth dust disk and is mostly confined within the disk. However, HCO^+ , H_2CO , HCN (and its isotopologues), and HNC (and DNC) reveal a bigger disk structure than $C^{17}O$. Figure 15 presents position-velocity (PV) diagrams for the $C^{17}O$ (left), H_2CO (middle), and HNC (right) lines along the semi-major axis of the disk as marked in their moment 1 maps in Figures 6. The HCN line is not used for a PV diagram along the semi-major axis because of its hyperfine structure (see the line profile in Figure 6). All three PV diagrams follow well the Keplerian rotation velocity profile, with a central mass of $1.2 M_{\odot}$.

On the other hand, as presented in Figure 16, the HCO^+ line seems to trace both the Keplerian disk (solid line) and the infalling rotating envelope (dashed line). The large arm-like structures seen in HCO^+ are a hint of the connection between the envelope and the Keple-

rian disk (see Section 4.1). The black contours in all PV diagrams are made using the PCA's first Principle Component (PC1) extracted from the COMs line data (Yun & Lee 2023). The PC1 provides very high S/N cube data, describing the representative spatial and velocity distribution of molecules (Okoda et al. 2021). As presented in Figure 4, all COMs emission is confined within the water sublimation radius in the disk. As a result, the most representative common feature of the COMs lines, which is the disk emission confined within the water sublimation radius, can be extracted by the PC1 of the PCA analysis of the COMs cube data.

4.3. Infall Signature

Direct evidence of infall is provided by red-shifted absorption against the continuum (Evans et al. 2015, inverse P-Cygni profile). We detect the inverse P-Cygni profile in the CO, HCO^+ , and HCN lines (Figure 17) extracted with an aperture of $1''$. The clear absorption negative dips are seen around 1.5 km s^{-1} . As mentioned in the previous section, in the PV diagrams of H_2CO and HNC, the negative features also appear at $\sim 1.5 \text{ km s}^{-1}$ (see the middle and right panels of Figure 15).

The infall features are also detected in the lower resolution ALMA observations of HCN 3–2 and HCO^+ 3–2 (Ruíz-Rodríguez et al. 2022). Their PV diagram of HCN along the semi-minor axis of the disk (P.A. $\sim 120^{\circ}$) shows a diamond-shape with the absorption feature, which could be reproduced by the infalling envelope within $2''$ (Tobin et al. 2012). The same feature is also shown in

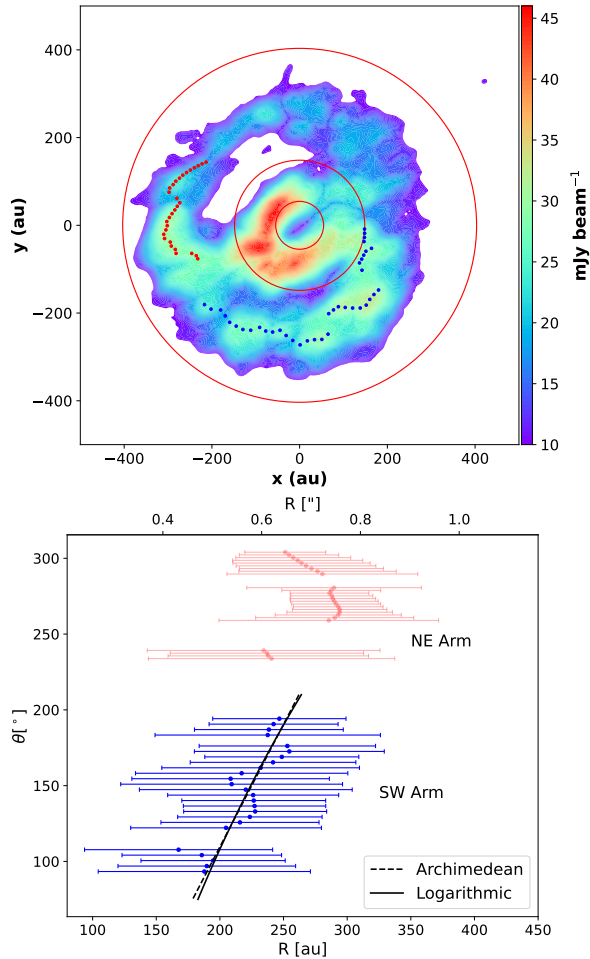


Figure 13. Deprojected moment 8 map of HCN and the peak positions of the spiral arms (top) and the spiral profiles of the two arms (bottom) using the inclination of 30 degrees. Three red circles in the deprojected moment 8 map denote the radii of $\ln r$ (au) = 4, 5, and 6, respectively. Only the SW arm (blue) has a spiral-like profile and can be fitted with an Archimedean or a logarithmic spiral.

the PV diagram of our HCN (see Figure 18) except for the resolution difference. Note that the maximum recoverable scale for the SG3 is $\sim 3.7''$ and the optically thick lines (CO, HCO⁺, and HCN) are partially filtered out in the channel of the absorption (~ 1.5 km s⁻¹).

4.4. High-Velocity Gas Components

In Figure 17, CO and HCO⁺ clearly show high-velocity wings at $|v| > 4$ km s⁻¹ (the gray shaded regions in the upper two panels), which is beyond the Keplerian rotation velocity expected at $r > 0.1''$. The contours in Figure 15 and 16, whose highest velocity is lower than 4 km s⁻¹, present the highest disk rotation velocity range that our observation can trace. Therefore, the high-velocity components detected in CO and HCO⁺ are not associated with the disk rotation. Although HCN may

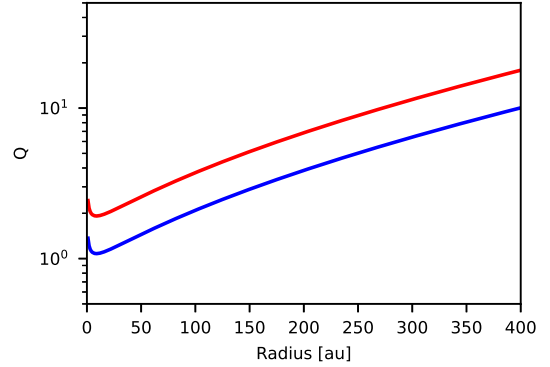


Figure 14. Toomre Q parameter for the V883 Ori disk. The red and blue lines indicate the Q parameters using the temperature distribution, $T(r) = 100$ K $\times \sqrt{r_{\text{snow}}/r}$, in the burst and the quiescent phase.

also trace the same high-velocity component (the bottom panel in Figure 17), it has confusion due to its hyperfine structure.

Figure 19 presents the moment 0 (contours) and 1 (images) maps of the high-velocity line components, and all of them are confined in the inner disk. Both red- and blue-shifted emissions for high-velocity CO components distribute along arm-like or corn-like structures, while the SO and HCO⁺ lines show only red-shifted high-velocity components, which are concentrated in the northeast part of the disk.

The CO velocity and morphological distribution are consistent with the larger outflow direction despite a small opening angle. We cannot, however, ignore the possibility of accreting flows. The SO and HCO⁺ high-velocity emission might be caused mainly by an accretion shock since the large arm-like structures, which are traced by the SO and HCO⁺ emission, are connected to the inner disk located inside the water sublimation radius.

5. A POSSIBLE SCENARIO FOR THE CURRENT ERUPTION IN V883 ORI

Table 4 summarizes the molecular tracers for various physical components detected in ALMA Band 6. The physical structures traced by different molecules could provide an opportunity to stitch those pieces of information together to understand the burst accretion process in V883 Ori.

The morphological (Section 3) and kinematical (Section 4) phenomena related to V883 Ori, which are traced by various molecular lines, suggest that during the quiescent phase, when the disk is still cold and marginally

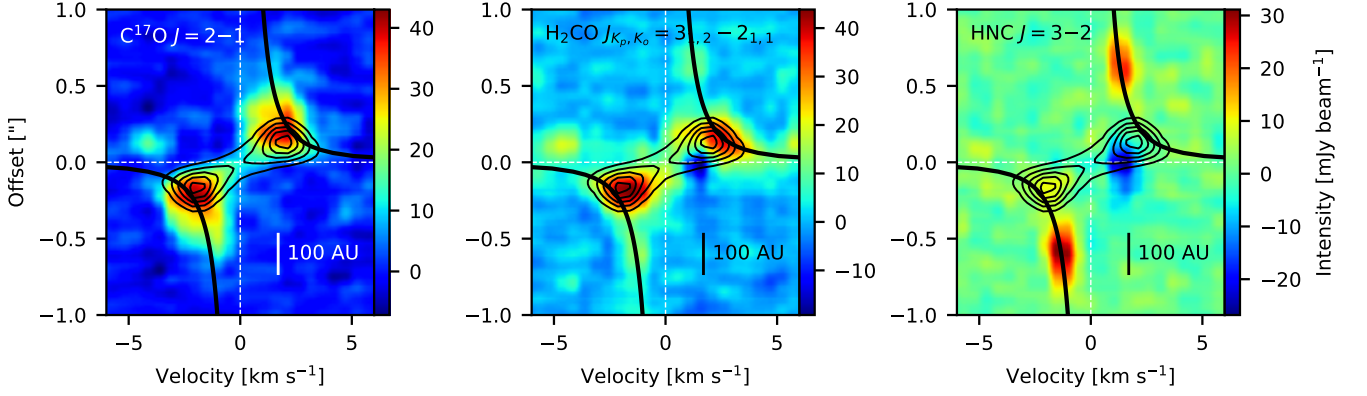


Figure 15. The position-velocity (PV) diagrams for $\text{C}^{17}\text{O } J=2-1$ (left), $\text{H}_2\text{CO } J_{K_p, K_o} = 3_{1,2} - 2_{1,1}$ (middle), and $\text{HNC } J=3-2$ (right). The black contours represent the PV diagram of COMs lines confined within the water sublimation radius. The solid black lines indicate the Keplerian rotation profile around the central mass of $1.2 M_\odot$. All PV diagrams are extracted from a line along the semi-major axis of the disk as marked in Figure 6. The blue-shifted blobs around -4 to -5 km s^{-1} between 0 to $0.2''$ are the red-shifted emissions of different adjacent lines. The negative values around 1.5 km s^{-1} provide evidence of infall motion; see Figure 17 for the HCO^+ and HCN line profiles with the infall signature, the inverse P-Cygni profile. The contours show the representative PV diagram of COMs.

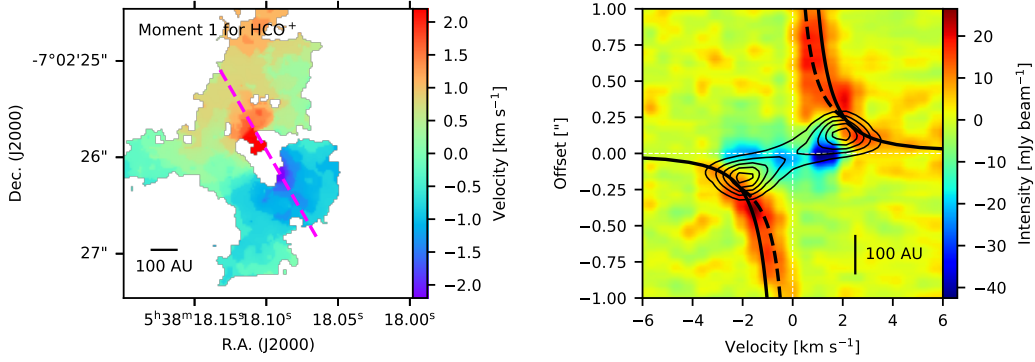


Figure 16. The PV-diagrams of $\text{HCO}^+ J=3-2$. The PV diagram is constructed along the magenta dashed line in the semi-major axis (left). The black contours in the PV-diagram are the same as in Figure 15. The black solid lines show the Keplerian rotation ($1/\sqrt{r}$), while the black dashed lines indicate a rotation profile ($1/r$) of the infalling and rotating envelope. The contours are the same as in Figure 15.

Table 4. Molecules tracing particular physical components in ALMA Band 6

Physical component	Molecules
Outflow cavity	CO
Infall signature	CO, HCO^+ , H_2CO , HCN, HNC
Arm-like structure in the envelope	HCO^+ , SO
Outer and inner disks connected by spiral arms	H_2CO , HCN
Outer disk boundary	HNC, DNC
Dust disk	C^{17}O
Water sublimation radius	HDO, HDCO, HNCO, OCS, H_2CCO , and COMs
Accretion shock at inner disk edge	SO_2 and high-velocity wings of HCO^+ and SO

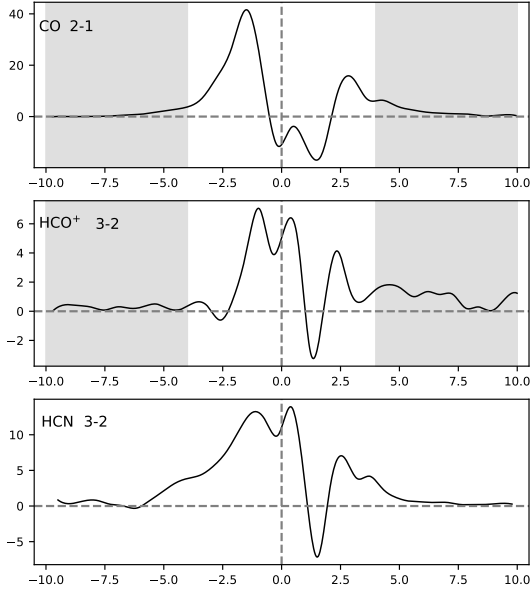


Figure 17. Spectra of CO, HCO⁺, and HCN, showing absorption below the continuum level. All spectra are extracted from a diameter of 1^{''}.

gravitationally unstable, the infall from the envelope to the outer disk through the large arms might have induced the spiral density wave in the disk. Then, the spiral wave propagated into the central regions of the disk to trigger the accretion burst (Bae et al. 2014), which, in turn, heated the disk, increasing the value of the Q parameter. Finally, the heated disk stabilized, and the spiral structures decayed. However, we still see the *residual* spiral structures in HCN and H₂CO because the timescale after the accretion burst may be much shorter than the chemical timescale within the disk, except at the dense disk midplane, which is well traced by the dust continuum and C¹⁷O emission. As a result, the chemical footprint along the spiral structures still remains visible on the disk.

6. SUMMARY

We carried out the ALMA Spectral Survey of An eruptive Young star, V883 Ori (ASSAY) in Band 6 with a resolution of 0.15^{''}~0.2^{''}. First of all, HDO was detected in the disk, demonstrating that COMs are sublimated along with water. In addition, our observations reveal that different molecules trace different physical components from the infalling envelope to the Keplerian disk, where the water sublimation radius is well resolved. The combination of various molecular emission distributions illustrates a possible scenario for the burst accretion process in V883 Ori. Except for HNC and DNC, all molecules emit within the water sublimation radius (~0.3^{''}) with an emission hole at the very

central part (<0.1^{''}) produced by high dust continuum opacity.

The inner disk shows a stronger emission in the southeast half because of the disk inclination; the southeast part faces us. The combination of dust opacity and disk inclination makes the molecular emission a crescent shape. The outer boundary of the gas disk is at r~0.8^{''}. Most molecular emission shows Keplerian rotation around a central source of 1.2 M_⊙, while moment 1 and 9 maps of HCO⁺, H₂CO, and HCN show inflow and spiral structures.

The 2-D emission distributions of simple molecules are explored in this work, and the summary (from larger scales to smaller scales) is as follows:

1. CO traces blue-shifted inner outflow cavity walls. The moment 1 map shows hints of inflows from envelope to disk;
2. HCO⁺ has an emission hole larger than expected from continuum opacity alone, and that is due to its destruction by H₂O. As a result, HCO⁺ traces the outer disk, producing a ring-like structure with an emission hole. Several arm features are connected with the ring-like structure. The velocity distribution along the arm structures is different from what is expected from the Keplerian rotation but rather consistent with the velocity of the infalling rotating envelope;
3. SO shows a compact emission inside the water sublimation radius with three weak but very prominent arm structures connected to the central emission region;
4. H₂CO covers the whole gas disk, but the emission inside the water sublimation radius is much stronger than the emission outside the water sublimation radius. The faint emission along the ring-like structure in the outer boundary of the disk shows spiral structures, which are similar to what is seen in HCN;
5. HCN has two distinct emission structures: one concentrates within the water sublimation radius, and the other distributes along the ring structure around the outer boundary of the dust disk. Spiral structures connect the central disk and the ring;
6. HNC and DNC present clearly a donut-shaped ring structure with missing emission within the water sublimation radius, probably due to its conversion to HCN at high temperature;

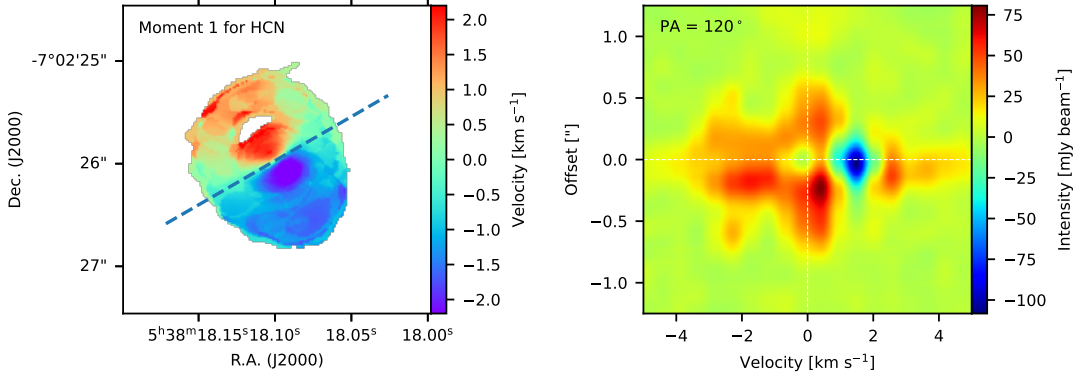


Figure 18. The PV-diagram of HCN (right) along the semi-minor axis as marked with the blue dashed line at the moment 1 map (left).

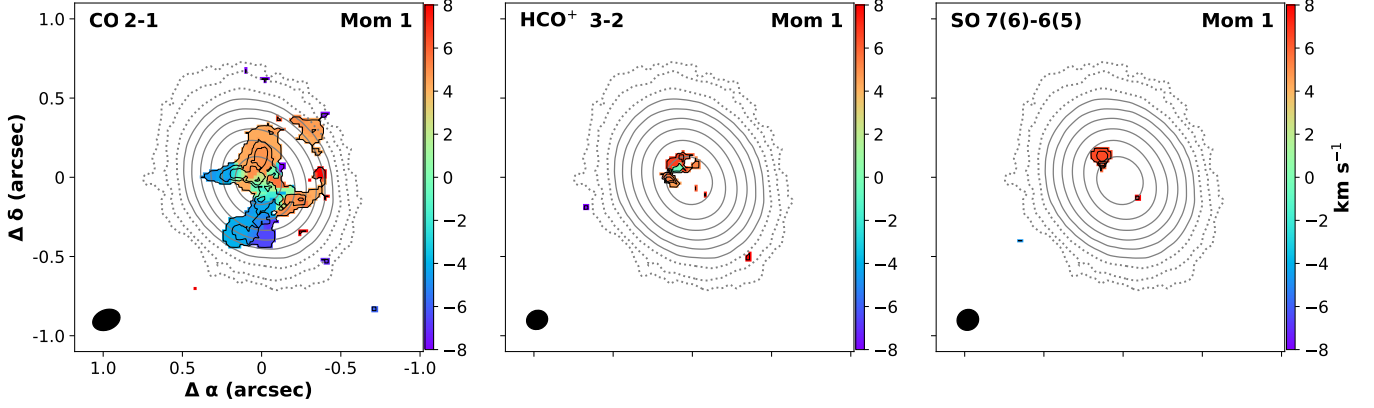


Figure 19. High-velocity components. Color images are moment 1 maps of CO, HCO⁺, and SO only for high-velocity wings ($4 < |v| < 10$ km s⁻¹). The black contour on top of color images indicates the moment 0 map of each molecule. The contour levels of the moment 0 map of CO are 6.4, 17.0, 27.6, and 38.2 mJy beam⁻¹ km s⁻¹. The contour levels of the moment 0 map of HCO⁺ are 5.7, 11.8, 17.9, and 24.0 mJy beam⁻¹ km s⁻¹. The contour levels of the moment 0 map of SO are 4.5, 6.2, 7.9, and 9.6 mJy beam⁻¹ km s⁻¹.

7. C¹⁷O traces the Keplerian smooth gas disk emission without substructure, except for the emission dip at the center caused by the high dust opacity. The size of the C¹⁷O disk is similar to the peak of HNC;
8. HDO directly proves the water sublimation radius, although H₂O transitions are not included within the frequency range covered by our spectral survey. The size of the HDO emission is about $\sim 0.3''$, corresponding to ~ 120 au;
9. CH₃OH and other COMs also distribute only within the water sublimation radius with stronger emission in the southeast part;
10. SO₂ and high-velocity wings of HCO⁺ and SO trace a shocked gas component, probably by the

infalling envelope along the arm-like structure, at the northern part of the inner disk.

7. ACKNOWLEDGEMENTS

We greatly appreciate the thorough and constructive review by the anonymous referee. The review significantly improved our paper. We appreciate Woong-Tae Kim and Jaehan Bae's helpful discussions on spiral structures. This work was supported by the National Research Foundation of Korea (NRF) grant funded by the Korean government (MSIT) (grant number 2021R1A2C1011718). S.L. is supported by a Korea Astronomy and Space Science Institute grant funded by the Korean government (MSIT) (Project No. 2024-1-841-00). G.J.H. is supported by general grants 12173003 and 11773002 awarded by the National Science Foundation of China. D.J. is supported by NRC Canada and by

an NSERC Discovery Grant. J.J.T. acknowledges support from NSF AST-1814762. L.C. is supported by the FONDECYT Regular program (grant No1211656) and the Millennium Nucleus YEMS (Code NCN2021_080) awarded by the Chilean government through the ANID agency. This research was supported by Basic Science Research Program through the National Research Foun-

dation of Korea(NRF) funded by the Ministry of Education(grant number RS-2023-00247790).

This paper makes use of the following ALMA data: ADS/JAO.ALMA#2019.1.00377.S. ALMA is a partnership of ESO (representing its member states), NSF (USA), and NINS (Japan), together with NRC (Canada), NSC and ASIAA (Taiwan), and KASI (Republic of Korea), in cooperation with the Republic of Chile. The Joint ALMA Observatory is operated by ESO, AUI/NRAO, and NAOJ.

REFERENCES

- Ahrens, V., Lewen, F., Takano, S., et al. 2002, *Zeitschrift Naturforschung Teil A*, 57, 669, doi: [10.1515/zna-2002-0806](https://doi.org/10.1515/zna-2002-0806)
- Alves, F. O., Caselli, P., Girart, J. M., et al. 2019, *Science*, 366, 90, doi: [10.1126/science.aaw3491](https://doi.org/10.1126/science.aaw3491)
- Bae, J., Hartmann, L., Zhu, Z., & Nelson, R. P. 2014, *ApJ*, 795, 61, doi: [10.1088/0004-637X/795/1/61](https://doi.org/10.1088/0004-637X/795/1/61)
- Bianchi, E., López-Sepulcre, A., Ceccarelli, C., et al. 2022, *ApJL*, 928, L3, doi: [10.3847/2041-8213/ac5a56](https://doi.org/10.3847/2041-8213/ac5a56)
- Cieza, L. A., Casassus, S., Tobin, J., et al. 2016, *Nature*, 535, 258, doi: [10.1038/nature18612](https://doi.org/10.1038/nature18612)
- Cieza, L. A., Ruíz-Rodríguez, D., Perez, S., et al. 2018, *MNRAS*, 474, 4347, doi: [10.1093/mnras/stx3059](https://doi.org/10.1093/mnras/stx3059)
- Díaz Rodríguez, A. K. 2021, PhD thesis, Institute of Astrophysics of Andalusia
- Esplugues, G. B., Viti, S., Goicoechea, J. R., & Cernicharo, J. 2014, *A&A*, 567, A95, doi: [10.1051/0004-6361/201323010](https://doi.org/10.1051/0004-6361/201323010)
- Evans, Neal J., I., Di Francesco, J., Lee, J.-E., et al. 2015, *ApJ*, 814, 22, doi: [10.1088/0004-637X/814/1/22](https://doi.org/10.1088/0004-637X/814/1/22)
- Fischer, W. J., Hillenbrand, L. A., Herczeg, G. J., et al. 2022, arXiv e-prints, arXiv:2203.11257. <https://arxiv.org/abs/2203.11257>
- Francis, L., Johnstone, D., Herczeg, G., Hunter, T. R., & Harsono, D. 2020, *AJ*, 160, 270, doi: [10.3847/1538-3881/abbe1a](https://doi.org/10.3847/1538-3881/abbe1a)
- Fraser, H. J., Collings, M. P., McCoustra, M. R. S., & Williams, D. A. 2001, *MNRAS*, 327, 1165, doi: [10.1046/j.1365-8711.2001.04835.x](https://doi.org/10.1046/j.1365-8711.2001.04835.x)
- Furlan, E., Fischer, W. J., Ali, B., et al. 2016, *ApJS*, 224, 5, doi: [10.3847/0067-0049/224/1/5](https://doi.org/10.3847/0067-0049/224/1/5)
- Graninger, D. M., Herbst, E., Öberg, K. I., & Vasyunin, A. I. 2014, *ApJ*, 787, 74, doi: [10.1088/0004-637X/787/1/74](https://doi.org/10.1088/0004-637X/787/1/74)
- Hacar, A., Bosman, A. D., & van Dishoeck, E. F. 2020, *A&A*, 635, A4, doi: [10.1051/0004-6361/201936516](https://doi.org/10.1051/0004-6361/201936516)
- Hartmann, L., & Kenyon, S. J. 1996, *ARA&A*, 34, 207, doi: [10.1146/annurev.astro.34.1.207](https://doi.org/10.1146/annurev.astro.34.1.207)
- Hirota, T., Yamamoto, S., Mikami, H., & Ohishi, M. 1998, *ApJ*, 503, 717, doi: [10.1086/306032](https://doi.org/10.1086/306032)
- Jin, M., Lee, J.-E., & Kim, K.-T. 2015, *ApJS*, 219, 2, doi: [10.1088/0067-0049/219/1/2](https://doi.org/10.1088/0067-0049/219/1/2)
- Jolliffe, I. T. 1986, Principal component analysis
- Kratter, K., & Lodato, G. 2016, *ARA&A*, 54, 271, doi: [10.1146/annurev-astro-081915-023307](https://doi.org/10.1146/annurev-astro-081915-023307)
- Lee, C.-F., Li, Z.-Y., & Turner, N. J. 2020, *Nature Astronomy*, 4, 142, doi: [10.1038/s41550-019-0905-x](https://doi.org/10.1038/s41550-019-0905-x)
- Lee, J.-E., Lee, S., Baek, G., et al. 2019, *Nature Astronomy*, 3, 314, doi: [10.1038/s41550-018-0680-0](https://doi.org/10.1038/s41550-018-0680-0)
- Lee, J.-E., Matsumoto, T., Kim, H.-J., et al. 2023, arXiv e-prints, arXiv:2306.06572, doi: [10.48550/arXiv.2306.06572](https://doi.org/10.48550/arXiv.2306.06572)
- Leemker, M., van't Hoff, M. L. R., Trapman, L., et al. 2021, *A&A*, 646, A3, doi: [10.1051/0004-6361/202039387](https://doi.org/10.1051/0004-6361/202039387)
- Long, F., Bosman, A. D., Cazzoletti, P., et al. 2021, *A&A*, 647, A118, doi: [10.1051/0004-6361/202039336](https://doi.org/10.1051/0004-6361/202039336)
- Mercimek, S., Podio, L., Codella, C., et al. 2023, *MNRAS*, doi: [10.1093/mnras/stad964](https://doi.org/10.1093/mnras/stad964)
- Miura, H., Yamamoto, T., Nomura, H., et al. 2017, *ApJ*, 839, 47, doi: [10.3847/1538-4357/aa67df](https://doi.org/10.3847/1538-4357/aa67df)
- Öberg, K. I., & Bergin, E. A. 2021, *PhR*, 893, 1, doi: [10.1016/j.physrep.2020.09.004](https://doi.org/10.1016/j.physrep.2020.09.004)
- Okoda, Y., Oya, Y., Abe, S., et al. 2021, *ApJ*, 923, 168, doi: [10.3847/1538-4357/ac2c6c](https://doi.org/10.3847/1538-4357/ac2c6c)
- Park, W., Lee, J.-E., Contreras Peña, C., et al. 2021, *ApJ*, 920, 132, doi: [10.3847/1538-4357/ac1745](https://doi.org/10.3847/1538-4357/ac1745)
- Pineda, J. E., Segura-Cox, D., Caselli, P., et al. 2020, *Nature Astronomy*, 4, 1158, doi: [10.1038/s41550-020-1150-z](https://doi.org/10.1038/s41550-020-1150-z)
- Ruíz-Rodríguez, D., Cieza, L. A., Williams, J. P., et al. 2017, *MNRAS*, 468, 3266, doi: [10.1093/mnras/stx703](https://doi.org/10.1093/mnras/stx703)
- Ruíz-Rodríguez, D. A., Williams, J. P., Kastner, J. H., et al. 2022, *MNRAS*, 515, 2646, doi: [10.1093/mnras/stac1879](https://doi.org/10.1093/mnras/stac1879)
- Sakai, N., Sakai, T., Hirota, T., et al. 2014, *Nature*, 507, 78, doi: [10.1038/nature13000](https://doi.org/10.1038/nature13000)

- Sánchez-Monge, Á., Schilke, P., Ginsburg, A., Cesaroni, R., & Schmiedeke, A. 2018, *A&A*, 609, A101, doi: [10.1051/0004-6361/201730425](https://doi.org/10.1051/0004-6361/201730425)
- Takami, M., Fu, G., Liu, H. B., et al. 2018, *ApJ*, 864, 20, doi: [10.3847/1538-4357/aad2e1](https://doi.org/10.3847/1538-4357/aad2e1)
- Thieme, T. J., Lai, S.-P., Lin, S.-J., et al. 2022, *ApJ*, 925, 32, doi: [10.3847/1538-4357/ac382b](https://doi.org/10.3847/1538-4357/ac382b)
- Tiné, S., Roueff, E., Falgarone, E., Gerin, M., & Pineau des Forêts, G. 2000, *A&A*, 356, 1039
- Tobin, J. J., Hartmann, L., Bergin, E., et al. 2012, *ApJ*, 748, 16, doi: [10.1088/0004-637X/748/1/16](https://doi.org/10.1088/0004-637X/748/1/16)
- Tobin, J. J., van't Hoff, M. L. R., Leemker, M., et al. 2023, *Nature*, 615, 227, doi: [10.1038/s41586-022-05676-z](https://doi.org/10.1038/s41586-022-05676-z)
- Toomre, A. 1964, *ApJ*, 139, 1217, doi: [10.1086/147861](https://doi.org/10.1086/147861)
- Tychoniec, L., van Dishoeck, E. F., van't Hoff, M. L. R., et al. 2021, *A&A*, 655, A65, doi: [10.1051/0004-6361/202140692](https://doi.org/10.1051/0004-6361/202140692)
- Valdivia-Mena, M. T., Pineda, J. E., Segura-Cox, D. M., et al. 2022, *A&A*, 667, A12, doi: [10.1051/0004-6361/202243310](https://doi.org/10.1051/0004-6361/202243310)
- van Gelder, M. L., Tabone, B., van Dishoeck, E. F., & Godard, B. 2021, *A&A*, 653, A159, doi: [10.1051/0004-6361/202141591](https://doi.org/10.1051/0004-6361/202141591)
- van 't Hoff, M. L. R., Tobin, J. J., Trapman, L., et al. 2018, *ApJL*, 864, L23, doi: [10.3847/2041-8213/aadb8a](https://doi.org/10.3847/2041-8213/aadb8a)
- van't Hoff, M. L. R., Harsono, D., Tobin, J. J., et al. 2020, *ApJ*, 901, 166, doi: [10.3847/1538-4357/abb1a2](https://doi.org/10.3847/1538-4357/abb1a2)
- Vorobyov, E. I., & Basu, S. 2005, *ApJL*, 633, L137, doi: [10.1086/498303](https://doi.org/10.1086/498303)
- . 2015, *ApJ*, 805, 115, doi: [10.1088/0004-637X/805/2/115](https://doi.org/10.1088/0004-637X/805/2/115)
- White, J. A., Kóspál, Á., Rab, C., et al. 2019, *ApJ*, 877, 21, doi: [10.3847/1538-4357/ab18fc](https://doi.org/10.3847/1538-4357/ab18fc)
- Yun, H.-S., & Lee, J.-E. 2023, *ApJ*, 958, 113, doi: [10.3847/1538-4357/acfa6a](https://doi.org/10.3847/1538-4357/acfa6a)

APPENDIX

A. INFORMATION OF THE OBSERVATION

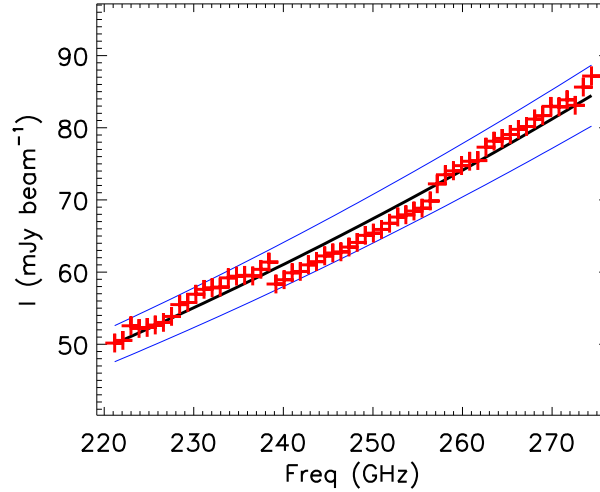


Figure A1. Intensity of the averaged continuum emission toward V883 Ori for the 60 SPWs. The red crosses indicate the continuum intensity. The black solid line indicates the best fit of the frequency and intensity in the log-log scales. The blue lines indicate the absolute errors of $\pm 5\%$. The self-calibration for each Science Goal makes the continuum intensities consistent with the Science Goals, and the scatter is lower than $\pm 5\%$.

Table A1. Image parameters

SGs	SPWs	Frequency ranges	b_{maj}	b_{min}	P.A.	RMS
		GHz	arcsec	arcsec	$^{\circ}$	mJy beam $^{-1}$
	1	220.70 – 221.64	0.15	0.13	-85.2	2.6
	2	221.61 – 222.55	0.16	0.13	-85.2	2.4
	3	222.52 – 223.45	0.17	0.13	-70.8	2.3
	4	223.42 – 224.36	0.15	0.13	-85.9	2.5
	5	224.33 – 225.26	0.17	0.13	-70.9	2.4
	6	225.23 – 226.17	0.17	0.13	-70.4	2.4
	7	226.14 – 227.08	0.16	0.13	-82.6	2.2
	8	227.05 – 227.98	0.16	0.13	-81.9	2.6
	9	227.95 – 228.89	0.18	0.13	-68.4	2.7
SG1	10	228.86 – 229.80	0.18	0.13	-69.0	2.3
	11	229.77 – 230.70	0.18	0.13	-68.7	2.5
	12	230.67 – 231.61	0.18	0.13	-69.8	2.9
	13	231.58 – 232.51	0.18	0.13	-69.1	2.8
	14	232.48 – 233.42	0.18	0.13	-69.1	2.5

Table A1 *continued*

Table A1 (*continued*)

SGs	SPWs	Frequency ranges	b_{maj}	b_{min}	P.A.	RMS
		GHz	arcsec	arcsec	°	mJy beam ⁻¹
	15	233.39 – 234.33	0.18	0.12	-68.9	2.9
	16	234.30 – 235.23	0.18	0.12	-69.0	2.8
	17	235.20 – 236.14	0.17	0.12	-75.9	3.5
	18	236.11 – 237.05	0.19	0.12	-68.7	2.5
	19	237.02 – 237.95	0.19	0.12	-68.8	3.0
	20	237.92 – 238.86	0.19	0.12	-68.8	3.0
	1	238.70 – 239.64	0.22	0.12	-79.7	2.8
	2	239.61 – 240.55	0.22	0.12	-79.9	2.0
	3	240.52 – 241.45	0.22	0.12	-80.1	2.2
	4	241.42 – 242.36	0.22	0.13	-81.1	2.3
	5	242.33 – 243.27	0.22	0.12	-78.6	2.3
	6	243.23 – 244.17	0.23	0.12	-79.0	2.4
	7	244.14 – 245.08	0.22	0.12	-78.8	2.2
	8	245.05 – 245.98	0.22	0.12	-79.8	2.3
	9	245.95 – 246.89	0.23	0.12	-77.6	2.3
SG2	10	246.86 – 247.80	0.23	0.12	-77.9	2.1
	11	247.77 – 248.70	0.23	0.12	-77.9	2.7
	12	248.67 – 249.61	0.23	0.12	-78.9	2.5
	13	249.58 – 250.52	0.24	0.12	-77.3	3.3
	14	250.48 – 251.42	0.23	0.12	-77.4	2.2
	15	251.39 – 252.33	0.23	0.12	-77.1	2.3
	16	252.30 – 253.23	0.23	0.12	-78.0	2.5
	17	253.20 – 254.14	0.23	0.12	-76.2	2.4
	18	254.11 – 255.05	0.23	0.12	-76.2	2.3
	19	255.02 – 255.95	0.23	0.12	-76.2	2.5
	20	255.92 – 256.86	0.23	0.12	-76.9	2.6
	1	256.70 – 257.64	0.13	0.11	-65.1	1.9
	2	257.61 – 258.55	0.13	0.11	-64.4	1.8
	3	258.52 – 259.45	0.13	0.11	-64.1	2.2
	4	259.42 – 260.36	0.13	0.12	-59.3	2.1
	5	260.33 – 261.27	0.14	0.13	-58.9	2.1
	6	261.24 – 262.17	0.14	0.13	-58.4	2.0
	7	262.14 – 263.08	0.14	0.13	-60.7	2.2
	8	263.05 – 263.99	0.14	0.13	-61.9	2.4
	9	263.95 – 264.89	0.14	0.12	-65.6	2.2
SG3	10	264.86 – 265.80	0.14	0.12	-67.4	2.0
	11	265.77 – 266.70	0.14	0.12	-68.2	2.2
	12	266.67 – 267.61	0.13	0.12	-68.1	2.6
	13	267.58 – 268.52	0.14	0.12	-69.5	2.4
	14	268.49 – 269.42	0.14	0.12	-70.8	2.1

Table A1 *continued*

Table A1 (*continued*)

SGs	SPWs	Frequency ranges	b_{maj}	b_{min}	P.A.	RMS
		GHz	arcsec	arcsec	°	mJy beam ⁻¹
	15	269.39 – 270.33	0.14	0.12	-71.2	2.3
	16	270.30 – 271.24	0.14	0.12	-72.3	2.5
	17	271.21 – 272.14	0.15	0.13	-79.6	2.3
	18	272.11 – 273.05	0.15	0.13	-74.7	2.5
	19	273.02 – 273.95	0.15	0.13	-75.9	2.8
	20	273.92 – 274.86	0.15	0.13	-75.8	2.9